Hindawi
International Journal of Photoenergy
Volume 2018, Article ID 7215843, 10 pages
https://doi.org/10.1155/2018/7215843

Research Article

Physics-Based Modeling and Experimental Study of Si-Doped InAs/GaAs Quantum Dot Solar Cells

A. P. Cédola,[1] D. Kim,[2] A. Tibaldi,[3] M. Tang,[2] A. Khalili,[1] J. Wu,[2] H. Liu,[2] and F. Cappelluti[1]

[1]*Department of Electronics and Telecommunications, Corso Duca degli Abruzzi 24, 10129 Torino, Italy*
[2]*Department of Electronic and Electrical Engineering, University College London, Torrington Place, London WC1E 7JE, UK*
[3]*Istituto di Elettronica e di Ingegneria dell'Informazione e delle Telecomunicazioni (IEIIT), Consiglio Nazionale delle Ricerche (CNR), Corso Duca degli Abruzzi 24, 10129 Torino, Italy*

Correspondence should be addressed to F. Cappelluti; federica.cappelluti@polito.it

Received 9 June 2017; Accepted 23 November 2017; Published 18 February 2018

Academic Editor: Urs Aeberhard

This paper presents an experimental and theoretical study on the impact of doping and recombination mechanisms on quantum dot solar cells based on the InAs/GaAs system. Numerical simulations are built on a hybrid approach that includes the quantum features of the charge transfer processes between the nanostructured material and the bulk host material in a classical transport model of the macroscopic continuum. This allows gaining a detailed understanding of the several physical mechanisms affecting the photovoltaic conversion efficiency and provides a quantitatively accurate picture of real devices at a reasonable computational cost. Experimental results demonstrate that QD doping provides a remarkable increase of the solar cell open-circuit voltage, which is explained by the numerical simulations as the result of reduced recombination loss through quantum dots and defects.

1. Introduction

Quantum dots (QDs) are being widely investigated since several years as a promising material for advanced concepts such as multiple junction [1], intermediate band [2, 3], and hot carrier [4] solar cells. The basic building block of such devices is typically made by an almost standard diode structure embedding a region with QDs. Electronic effects and charge transfer mechanisms in the QDs and between the QD localized states and the continuum states of the host semiconductor present quantum mechanical features, while a large part of the device is made by bulk regions working in the semiclassical transport regime. Thus, device level simulation models of QD solar cells inherently require multiscale approaches which shall be able to combine the micro- and macroscale description at an affordable computational cost [5].

In the hierarchy of multiscale models for the simulation of QD solar cells (QDSCs), one of the simplest approaches is provided by spatially resolved rate equation-based models, which couple microscopic calculated quantities such as the QD electronic structure, optical properties, and scattering rates to macroscopic equations for transport in the extended states. Several of the QD model parameters can also be extracted from routinary experimental data, making such approach suitable for both design and interpretation purposes. Modelling approaches able to reproduce the behavior of realistic devices and analyze the interplay of the involved physical mechanisms allow gaining insight into experimental results and provide useful feedback to the technology development. In this respect, while detailed balance theory of QDSCs has received a lot of attention and is useful to indicate the long-term target efficiency [6–8], less effort has been devoted to models based on semiconductor transport equations [9–13] and to the implications of QD carrier dynamics on the photovoltaic performances [14]. On the other hand, previous work by some of the present authors has shown

that introducing a proper description of interband and intersubband QD dynamics is a crucial asset to address some of the most critical issues encountered in QDSCs, such as poor carrier collection efficiency and degradation of the open-circuit voltage [15, 16].

In this work, we apply the QD-*aware* physics-based model firstly proposed in [15] to the study of InAs/GaAs QDSC exploiting selective Si doping. QD doping is extensively investigated as an attractive means to control photocarrier dynamics and improve QDSC performance (see, e.g., the recent review in [17] and the references therein). The present work extends the analysis already proposed in [18] on the interplay between doping and recombination processes in QDSCs and provides an experimental-based validation to the conclusions in [18]. To ensure an accurate description of the cell behavior, the model in [15, 18] has been complemented by an accurate electromagnetic model for carrier photogeneration. In the following, we present the basic ideas of the model, highlighting its thermodynamic consistency and discussing the identification of microscopic parameters from quantum models and experimental characterization, and we show with a real case study the valuable insight into device behavior that can be gained with this simulation approach.

2. Model

QD-based solar cells usually exploit a $p-n$ or $p-i-n$ structure with a region including a periodic stack of QD layers. Figure 1 schematically shows the energy band diagram of an In(Ga)As QD surrounded by GaAs barriers and the carrier transfer processes that are included in the model, as discussed in the following. From the electronic standpoint, the 3D confinement gives rise to a deeply confined energy level, the ground state (GS), one or more excited states (ES), both of them with 0D density of states, and a quasi-two-dimensional (2D) energy state associated with the wetting layer (WL) [19]. At device level, the WL subband is described as a 0D level with high degeneracy factor, accounting for the 2D density of states of the WL and the weakly confined excited states.

We assume negligible coupling between the QD layers; thus, the exchange of carriers between localized states in different layers is always mediated by the barrier extended states. Under such hypothesis, the QDSC operation is as follows: electrons and holes are photogenerated in the barrier and QD states by above- and below-gap photons, respectively. Charge transfer between continuum and bound states is characterized by capture and escape processes through the WL level. In the barrier, carriers move by drift-diffusion, and when they arrive within the interaction range of the QD region (a few nanometers), they can be either emitted through the QD layer or captured in the QD states. Dually, confined carriers may escape from the QD states through thermal emission to the WL and from the WL to the barrier. Only thermal escape is considered in this work, because in the QDs under study, at room temperature, photon-assisted escape is negligible [20]; moreover, due to the shallow confinement, thermal emission is so efficient that the inclusion of an electric field-assisted mechanism does not provide any significant change to the overall picture. In [15], a good correlation between simulated and measured open-circuit voltage of cells with QD ground state emission between 1000 nm and 1300 nm has been demonstrated. On the other hand, deeper QDs may be significantly affected by field-assisted tunneling. Thus, the model formulation described in the following shall be applied only to the study of relatively shallow QDs at room temperature, hereinafter referred as thermally limited operation.

The electrical problem is formulated in terms of electrostatics and free carrier continuity equations, accounting for charge localization due to the QDs and charge transfer mechanisms between barrier and bound states. At the QD layer, Poisson's equation and electron continuity equation (for the sake of brevity, we omit hole equations) read as

$$\begin{aligned} \frac{\partial}{\partial x}\left(\in \frac{\partial \phi}{\partial x}\right) &= -q\left[p - n + \sum_{\gamma}\left(p_{\gamma} - n_{\gamma}\right) + N_D^{+} - N_A^{-}\right], \\ \frac{\partial n}{\partial t} &= \frac{1}{q}\frac{\partial J_n}{\partial x} - U_{\mathrm{B}} + G_{\mathrm{B}} - U_{n,\mathrm{CAP}}, \end{aligned} \tag{1}$$

where ϕ is the electrostatic potential, n and p are the electron and hole densities, respectively, in the barrier, n_{γ} and p_{γ} are the electron and hole densities, respectively, in the QD state γ, and N_D^{+} and N_A^{-} are the ionized donor and acceptor density, respectively. In the continuity equation, J_n is the electron drift-diffusion current density, U_{B} the net recombination rate, G_{B} the band-to-band photogeneration rate, and $U_{n,\mathrm{CAP}}$ the WL-mediated net capture rate from the barrier into the QD states, that is, the difference between the capture rate from barrier to WL and the escape rate from WL to barrier. U_{B} includes both radiative and nonradiative processes. Radiative recombination is modeled as

$$U_{\mathrm{B,r}} = B_{\mathrm{op}}\left(pn - n_i^2\right), \tag{2}$$

B_{op} being the GaAs spontaneous emission coefficient and n_i the thermal equilibrium carrier density. Nonradiative recombination follows the Shockley-Read-Hall theory

$$U_{\mathrm{B,nr}} = \frac{pn - n_i^2}{\tau_p(n + n_1) + \tau_n(p + p_1)}, \tag{3}$$

where $\tau_{n(p)}$ is the SRH recombination lifetime and n_1 and p_1 are the electron and hole densities, respectively, when Fermi level corresponds to the trap energy level, here assumed at midgap.

Capture and cascaded relaxation processes are described by a set of rate equations establishing a detailed balance, for each QD level, among all the interband and intersubband charge transfer mechanisms. At each QD layer, the rate equation describing the electron population in the subband γ reads as

$$\frac{\partial n_{\gamma}}{\partial t} = U_{n,\mathrm{CAP}}^{\gamma+1\to\gamma} - U_{n,\mathrm{CAP}}^{\gamma\to\gamma-1} - U_{\gamma} + G_{\gamma}, \tag{4}$$

where $U_{\gamma} \approx f_{n,\gamma} f_{p,\gamma}/\tau_{r,\gamma}$ and G_{γ} are the net interband radiative recombination and photogeneration rates of the γ subband

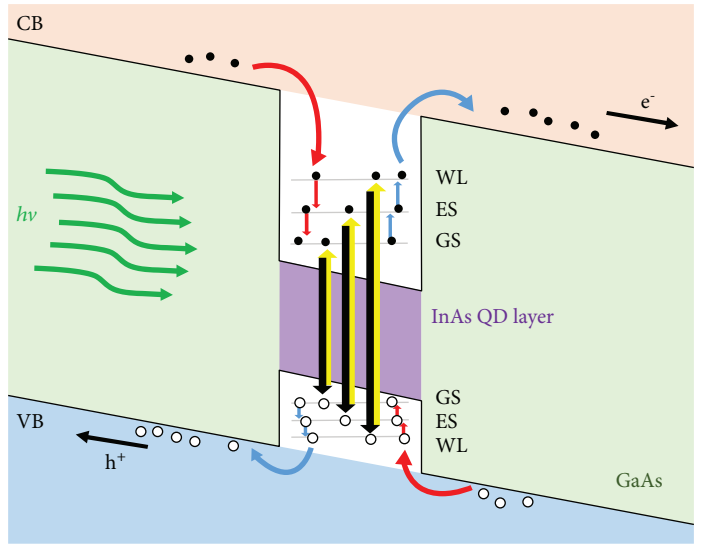

FIGURE 1: Energy band diagram of one InAs QD layer embedded in GaAs including all the carrier processes considered in the model: capture/relaxation (red), escape (blue), photogeneration (yellow), and recombination (black). WL is treated as a 0D state.

state (γ = WL, ES, GS), respectively. For the sake of simplicity, we consider only the radiative transitions associated to electron and hole states in the same subband. A radiative lifetime of 1 ns is assumed for all the QD states. The term $U_{n,\mathrm{CAP}}^{\gamma\to l}$ is the net capture rate from the intersubband state k to the l one. Note that capture and relaxation processes are allowed to exist only between adjacent energy levels; thus, for γ = WL, $\gamma+1$ state indicates the barrier, whereas for γ = GS the terms involving $\gamma-1$ must be ignored. To make the formulation treatable, we assume in the following Maxwell-Boltzmann statistics for the continuum states and Fermi-Dirac statistics for the QD states. Moreover, we neglect QD inhomogeneous broadening; thus, the QD density of states is a Dirac delta function.

The capture or relaxation process of an electron from state γ to state $\gamma-1$ can be formulated as

$$R_{\mathrm{CAP}} = c' N_\gamma f_\gamma N_{\gamma-1}\left(1-f_{\gamma-1}\right), \tag{5}$$

where c' is the scattering rate ($\mathrm{cm}^3\cdot\mathrm{s}^{-1}$) of the transition and N_k is the effective density of states in the k band, with distribution function f_k. The reverse escape process reads as

$$\begin{aligned} R_{\mathrm{ESC}} &= e' N_{\gamma-1} f_{\gamma-1} N_\gamma \left(1-f_\gamma\right) \\ &= e' N_{\gamma-1} N_\gamma f_\gamma \left(1-f_{\gamma-1}\right) e^{\left(E_{Fn}^{\gamma-1}-E_{Fn}^{\gamma}\right)/k_BT} e^{\left(E_\gamma-E_{\gamma-1}\right)/k_BT}, \end{aligned} \tag{6}$$

where the last term is derived taking advantage of the following identity, which holds regardless of the specific statistics, Boltzmann or Fermi [21],

$$f_\gamma\left(1-f_{\gamma-1}\right)e^{\left(E_{Fn}^{\gamma-1}-E_{Fn}^{\gamma}\right)/k_BT} = f_{\gamma-1}\left(1-f_\gamma\right)e^{\left(E_{\gamma-1}-E_\gamma\right)/k_BT}. \tag{7}$$

In (6), E_k and E_{Fn}^k are the energy of the k state and the quasi-Fermi level of the corresponding electron population, respectively. For barrier electrons, obviously, E_k coincides with the minimum of the conduction band. The detailed balance at thermal equilibrium imposes

$$c' = e' e^{\left(E_\gamma-E_{\gamma-1}\right)/k_BT}, \tag{8}$$

yielding the net capture rate $U_{n,\mathrm{CAP}} = R_{\mathrm{CAP}} - R_{\mathrm{ESC}}$

$$U_{n,\mathrm{CAP}}^{\gamma\to\gamma-1} = \frac{1}{\tau_{\mathrm{cap}}^{\gamma-1}} n_\gamma \left(1-\frac{n_{\gamma-1}}{N_{\gamma-1}}\right)\left(1-e^{\left(E_{Fn}^{\gamma-1}-E_{Fn}^{\gamma}\right)/k_BT}\right), \tag{9}$$

$n_k = N_k f_k$ being the free electron density in the k state and $\tau_{\mathrm{cap}}^{\gamma} = 1/c' N_{\gamma-1}$. Equation 9 highlights the correlation between the onsets of capture ($U_{n,\mathrm{CAP}} > 0$) or escape ($U_{n,\mathrm{CAP}} < 0$) and the nonequilibrium condition between electron populations in the states E_γ and $E_{\gamma-1}$.

The above formulation can be generalized so as to include the detailed energy dependence of the density of states of the different subbands (e.g., to include a more physical description of the QD states and WL states), Fermi-Dirac statistics in the continuum bands, as well as the energy dependence of the microscopic scattering matrix element $M^{\gamma,\gamma-1}$ describing the interaction between the two states [21]:

$$\begin{aligned} R_{\mathrm{CAP}} &= \int_{E_\gamma} dE'_\gamma \int_{E_{\gamma-1}} g_\gamma\left(E'_\gamma\right) f_\gamma\left(E'_\gamma\right) M^{\gamma,\gamma-1} g_{\gamma-1}\left(E'_{\gamma-1}\right) \\ &\quad \cdot \left(1-f_{\gamma-1}\left(E'_{\gamma-1}\right)\right) dE'_{\gamma-1}, \\ R_{\mathrm{ESC}} &= \int_{E_\gamma} dE'_\gamma \int_{E_{\gamma-1}} g_\gamma\left(E'_\gamma\right)\left(1-f_\gamma\left(E'_\gamma\right)\right) M^{\gamma-1,\gamma} g_{\gamma-1} \\ &\quad \cdot \left(E'_{\gamma-1}\right) f_{\gamma-1}\left(E'_{\gamma-1}\right) dE'_{\gamma-1}. \end{aligned} \tag{10}$$

Introducing the energy averaged scattering element $\langle M^{\gamma,\gamma-1}\rangle$, averaged over the entire ensemble of possible

initial and final states, and after some analytical manipulation, one derives an expression of $U_{n,\mathrm{CAP}}$ completely analogous to 8, with $\tau_{\mathrm{cap}}^{\gamma-1} = 1/\langle M^{\gamma,\gamma-1}\rangle N_{\gamma-1}$, $n_\gamma = \int_E g_\gamma f_\gamma dE$, $N_{\gamma-1} = \int_E g_{\gamma-1} dE$.

Capture and relaxation in self-assembled In(Ga)As/GaAs QDs happen through complicated dynamics involving emission of longitudinal optical (LO) phonon emission, polaron (electron-phonon coupling) decay, defect-mediated relaxation, carrier-carrier scattering, and so forth (see, e.g., [22–24] and the references therein). The scattering time τ_{cap} derived from quantum models is typically a function of the carrier density in the WL and QD states, which in turn depends on injection/photogeneration of carriers according to the cell operating conditions and on design parameters such as doping. At low carrier density, electron-LO-phonon interaction and Auger electron-hole scattering act as very efficient relaxation channels, providing relaxation times on the scale of tenths of ps to tens of ps [22, 23, 25]. At high carrier density, carrier-carrier scattering may become significant, yielding again relaxation times on the ps scale [24]. In particular, for n-doped (p-doped) QD hole (electron), the population is extremely low; thus, electron-hole scattering is negligible and relaxation occurs through a combination of electron-electron (hole-hole) scattering and carrier-LO-phonon relaxation. These predictions are confirmed by several experimental data on undoped and doped samples: in [26], relaxation times from WL to QD ground state were found to be 2, 3, and 6 ps for p-doped, n-doped, and undoped samples, respectively. Further experimental data of similar sign are summarized in [23]. Overall, theoretical and experimental results on In(Ga)As/GaAs QDs show that net capture/relaxation rates—on a ps scale—are extremely fast with respect to the characteristic QD band-to-band and intraband radiative lifetimes (about 1 ns and 100 ns, resp. [25]), making the QD carrier lifetime largely dominated by the QD radiative lifetime. Moreover, the open-circuit voltage (V_{oc}) penalty in thermally limited QDSCs is dominated by the ratio between carrier lifetime in the barrier and carrier lifetime in QDs [27], the last one being the net result of the competing processes of capture/relaxation/recombination through the QDs—from the one hand—and escape from the QD bound states and electric-field-driven sweep out through the extended states—from the other hand. Thus, at least in In(Ga)As/GaAs QDs and under nonconcentration operation, capture/relaxation times can be reasonably treated as constant parameters, neglecting their carrier density dependence and the possible electric-field dependence due to tunneling mechanisms. In this respect, it may be remarked that the electrical field across the interdot layers plays however an important role in the resulting net capture rate in QDs: at high field, free-carrier transit time is high and the probability of capture from the barrier into the QDs remains low (such situation is representative of the short-circuit condition, where QD recombination turns to be negligible). In [28], carrier capture from the GaAs barrier was found to be fully quenched in fields of only 15 kV/cm. When the electrical field is significantly screened (e.g., as forward bias approaches the maximum power point and open-circuit voltage), the transit time decreases and the net capture rate in the QDs increases; that is, QDs turn into radiative trap centers (see [15, 16] for a detailed discussion).

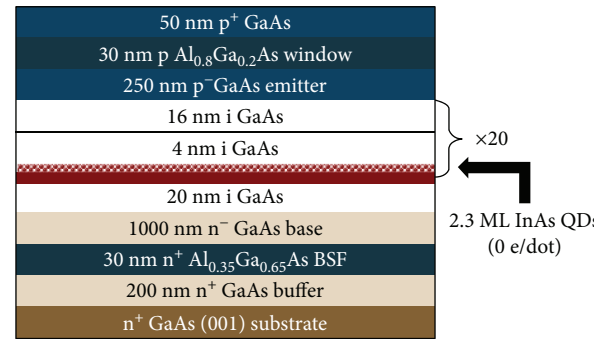

Figure 2: Sketch of the epilayer structure of the 20 × QD solar cell (R3 and R4 samples).

In the following simulations, we use empirical data extracted in [15] from the interband-pump-intraband-probe spectroscopy experiments reported in [29]. To this aim, we assume very fast capture into the WL, which occurs through one-LO-phonon interaction on a 0.1 ps time scale, followed by cascaded relaxation of carriers into the ES and GS states. Fitting the time-resolved IR absorption of QDs similar to those in the present work, we estimated electron time constants of about 1 ps [15] for WL-ES and ES-GS relaxation. Due to their large effective mass, holes form closely spaced energy levels, characterized by fast phonon-mediated capture and relaxation mechanisms, whose time constants are set to 100 fs.

Concerning the photogeneration rates, the simulation calculates the (optical) electric field profile across the multilayer structure, with each material characterized by the complex refractive index $\hat{n} = n + i\kappa = n + i\alpha\lambda/(4\pi)$ (α being the absorption coefficient), exploiting a scattering matrix formalism for coherent multilayers [30]. From the optical electric field profile $E_{\mathrm{op}}(x)$, the absorbed photon density (at each wavelength) and the photogeneration rate (assuming unitary quantum yield) are then calculated through the divergence of the Poynting vector, yielding

$$G = \frac{\sigma}{2h\nu}\left|E_{\mathrm{op}}\right|^2, \tag{11}$$

where $h\nu$ is the photon energy and $\sigma = n\alpha/\mu_0 c$ the electrical conductivity (μ_0 and c being the vacuum magnetic permeability and light velocity, resp.).

The model numerical implementation is based on the discretization of the electrical equations through the Scharfetter-Gummel scheme and the self-consistent solution of the resulting system of nonlinear equations through Newton-based methods [31].

3. Experimental

All the epitaxial structures were grown using a solid-source molecular beam epitaxy (MBE) on n^+ GaAs (100) substrates. InAs/GaAs QDSC structures based on those previously demonstrated by Kim et al. [32] were used, as shown in Figure 2. The structures consist of a 200 nm GaAs buffer layer with Si

doping density of $1 \times 10^{18}\,\text{cm}^{-3}$, 30 nm $Al_{0.35}Ga_{0.65}As$ back surface field (BSF) with Si doping density of $1 \times 10^{18}\,\text{cm}^{-3}$, 1000 nm GaAs base with Si doping density of $1 \times 10^{17}\,\text{cm}^{-3}$, 250 nm GaAs emitter with Be doping density of $2 \times 10^{18}\,\text{cm}^{-3}$, 100 nm GaAs emitter with Be doping density of $5 \times 10^{18}\,\text{cm}^{-3}$, 30 nm $Al_{0.75}Ga_{0.25}As$ window layer with Be doping density of $2 \times 10^{18}\,\text{cm}^{-3}$, and 50 nm GaAs contact layer with Be doping density of $1 \times 10^{19}\,\text{cm}^{-3}$. 20 layers of InAs QDs were grown in the intrinsic region of the SCs. The QDs were grown by the Stranski-Krastanov mode with the InAs coverage of 2.1 monolayers (ML) at a substrate temperature of ~500°C. A high growth temperature was used during the growth of the GaAs spacer layers to suppress the formation of dislocations [33–35]. No cap layer was applied between the InAs QDs and the GaAs space layers. Direct Si doping with doping densities of 14 e/dot was applied to the QDs in the Si-doped QDSCs [32]. Whereas the InAs QD layers in all other samples were separated by 20 nm GaAs spacer, the spacer layers in the QDSC with additional spacer layers (R5) were 25 nm each, which gave additional 100 nm in total. For the post-growth sample cleaning, the SCs were ultrasonicated in acetone and isopropanol for 10 min each at room temperature. To remove the oxide on the surface of the samples, the SCs were immersed in diluted ammonia solution (1 : 19) for 30 s. A Au-Zn alloy (95% Au, 5% Zn) was deposited in grid patterns to form 200 nm thick *p*-type electrodes using a metal shadow mask and a thermal evaporator.

The morphology of the QD layers was studied using a Veeco Nanoscope V atomic force microscope (AFM). 532 nm excitation from a diode-pumped solid-state laser was used for photoluminescence (PL) measurements. The sample temperature during the PL measurements was controlled using a He-cooled cryostat. Current density versus voltage ($J-V$) measurements was performed using an LOT-calibrated solar simulator with a xenon lamp under one-sun air mass (AM) 1.5 G illumination at 25°C. The devices were connected to a Keithly 2400 sourcemeter via a 4-point probe station, and ReRa Tracer 3 software was used to collect the data. Photocurrent measurements were obtained using a Halogen lamp chopped to 188 Hz through a Newport monochromator. A 4-point probe connected with a lock-in amplifier was used to collect data. The monochromatic beam was then calibrated using a Si photodiode, and the data was analysed with Photor QE 3.1 software to produce the external quantum efficiency (EQE).

4. Results and Discussion

An overview of the photovoltaic characteristics of the undoped and Si-doped QD solar cells and of an undoped reference cell (same geometry and doping but without the inclusion of QDs) is presented in Figure 3 and Table 1. The target performances for the REF cell were $V_{oc} = 1.04$ V, short circuit current density (J_{sc}) of 14.2 mA/cm^2, and fill factor (FF) of 86.5%. All the cells, included in the REF one, show quite low FF and unusual rounded shape of the $J-V$ characteristic, whose origin is attributed to issues in the realization of the metal grid. The observed behavior cannot be fitted by a simple lumped model with series and shunt resistances: a nonuniform three-section model of the cell [36] provides a good fitting of the measured characteristics, as shown in Figure 3, with extracted series resistances of about 50, 1, and 1 Ωcm^2 for each subcell. The undoped QDSC shows a marked penalty of V_{oc} with respect to the REF cell, which is partially recovered in the samples with directly doped QDs. On the other side, the doped QDSCs have lower J_{sc} that can be in part attributed to the shrinking of the space charge region and subsequent reduction of carrier collection and in part to lower minority carrier lifetime in the base and emitter regions as demonstrated later (see Figure 4) based on measured EQE and simulations. In may be worth noticing that under the assumption of similar material quality, the slightly larger thickness of the undoped region of the R5 sample (520 nm) with respect to the R4 one (420 nm) would produce an absolutely marginal difference in terms of device level behavior. Finally, the higher J_{sc} of the undoped QDSC with respect to the REF cell is not related to QD photogeneration but rather to a worse carrier collection efficiency in the emitter causing a decreased EQE in the GaAs absorption range.

The electronic structure of QDs is estimated based on room temperature steady-state PL. The measured PL spectra at low and room temperature are shown in Figures 5(a) and

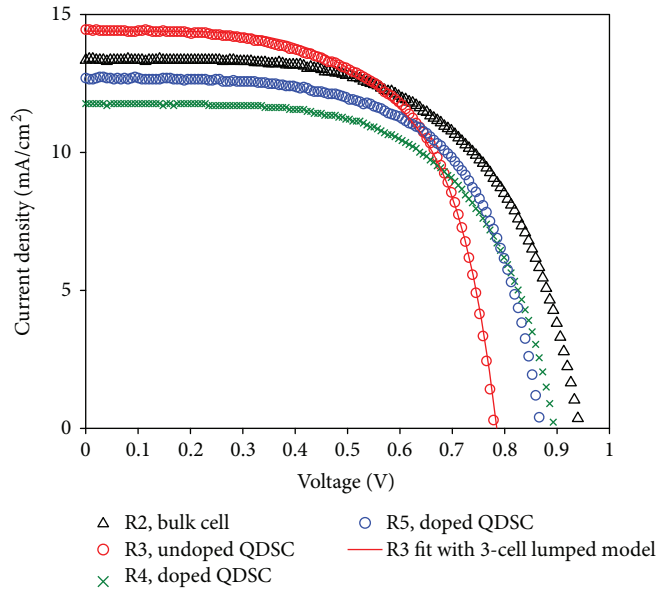

Figure 3: Current density versus voltage characteristics measured under one-sun illumination (AM 1.5 G) for the reference GaAs bulk cell (R2), undoped QDSC (R3), and two-doped (14 e/dot) QDSC with interdot spacing of about 20 nm (R4) and 25 nm (R5).

Table 1: Photovoltaic parameters extracted from the measured $J-V$ characteristics in Figure 3.

Device	J_{sc}, mA/cm^2	V_{oc}, V	FF, %
R2, REF GaAs cell	13.37	0.942	59.7
R3, undoped QD	14.42	0.778	62.7
R4, doped QD	11.74	0.894	61.1
R5, doped QD	12.70	0.868	63.1

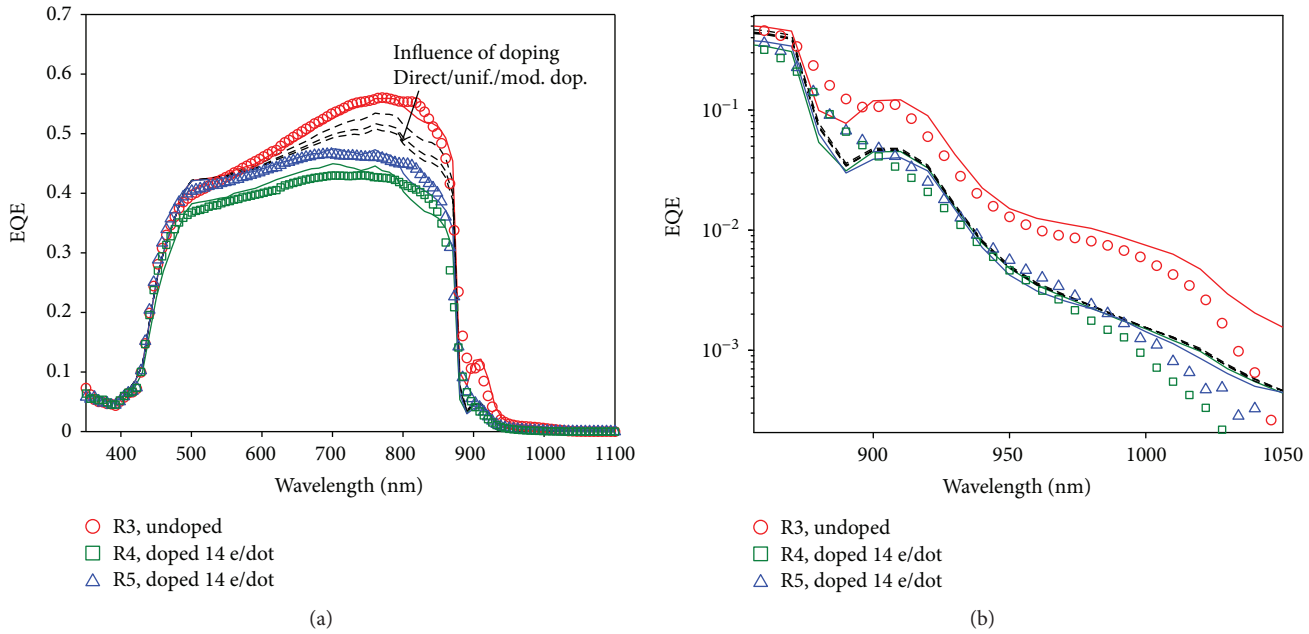

FIGURE 4: (a) Comparison between measured and simulated EQE. (b) Zoom in the QD wavelength region. The black dashed lines show the predicted decrease of EQE according in the doped (14 e/dot) QD solar cell assuming the same minority carrier lifetime as in the undoped sample and under different hypotheses of dopant impurity distribution: well confined in the QD region (direct), uniformly distributed across the QD stack, and located at the center of the GaAs interdot layers. Symbols show experimental data. Solid lines inidicate simulation and best fit.

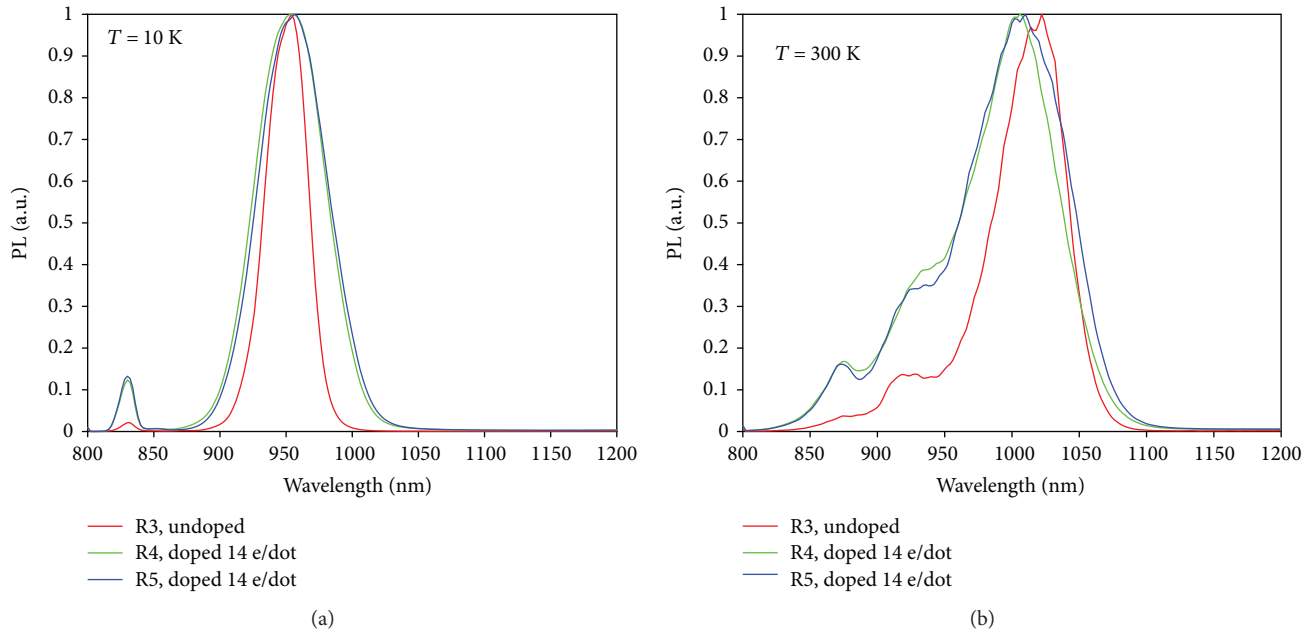

FIGURE 5: Normalized PL spectra measured at $T = 10$ K (a) and $T = 300$ K (b).

5(b), respectively. At low temperature, only the GS state is visible, with a slight redshift of the PL peak and an increase of the full width at half maximum (FWHM) for the doped samples with respect to the undoped one especially in the longer wavelength region. The observed behavior suggests that in the doped samples the distribution of the dot size is less homogeneous, with an increased density of larger (i.e., more confined) QDs which emit at lower energies [37]. At 300 K, the slight blue shift of the GS emission of the doped samples may be indicative of a higher interband transition energy and of a weaker quantum confinement of electrons in the GS. More importantly, the PL spectrum makes well visible the increase of the WL emission with respect to the GS one with doping. This indicates less efficient ES and GS

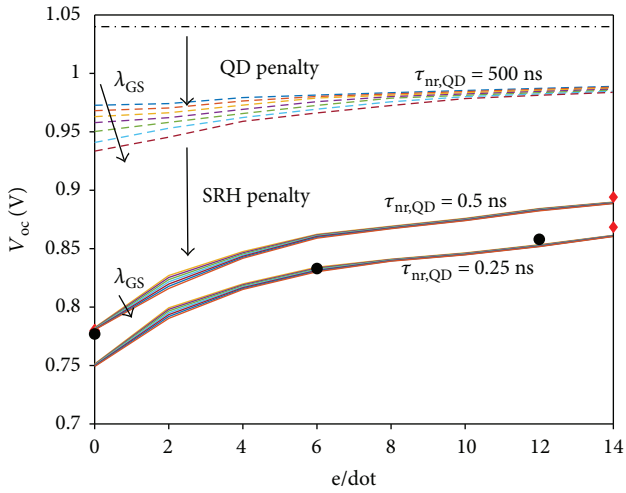

FIGURE 6: Analysis of V_{oc} penalty in QDSC as a function of the per dot doping density, for different GS energy confinement (λ_{GS} ranges from 990 nm to 1050 nm) and different minority carrier lifetime in the interdot layers ($\tau_{nr,QD}$). The black dash-dot line indicates the V_{oc} of the reference bulk GaAs cell. The red bullet indicates experimental data in this work. The black bullet indicates experimental data from Lam et al. [43].

relaxation pathways for the WL state of doped QDSCs that can be understood as a consequence of blocking of electron relaxation in the ES and GS due to state filling effects [18]. From the PL measurements, we identified energy gaps of 1.24 eV, 1.28 eV, and 1.37 eV for GS, ES, and WL, respectively, as representative values for all the samples under study. The impact of slight variations in the QD electronic structure and GS energy is analyzed in detail later (see Figure 6), based on the analysis of V_{oc} data. Based on literature data [38], the confinement energy for electron and holes in each state is set to 80% and 20% of the difference between barrier and QD level energy gap [38] (e.g., $\Delta E^{e}_{GS} = 0.8(E_g - E_{g,GS})$, E_g and $E_{g,GS}$ being the barrier energy gap and GS energy gap, resp.).

The analysis of the experimental results through the device level model in Section 2 provides also an estimation of the Shockley-Read-Hall lifetimes in (3) characterizing nonradiative recombination across the barrier states. Even though the strong interaction between continuum and localized states makes not obvious to single out the impact of such parameters on the cell photovoltaic behavior, some basic knowledge of device operation (as routinely observed in bulk cells) allows identifying a suitable strategy for their extraction. In fact, it is worth reminding that short-circuit SRH recombination is more detrimental in the doped regions, whereas it marginally affects carrier collection efficiency in the undoped one. In contrast, at open-circuit condition, the most detrimental loss arises from SRH recombination in the undoped region. Thus, once a reasonably accurate optical model of the cell is established, the analysis of EQE spectra—in particular in the GaAs wavelength range—allows identifying lower bounds for the SRH lifetimes in the base and emitter, whereas the analysis of the open-circuit voltage provides an estimation of SRH lifetimes in the undoped region.

The measured EQE spectra are shown in Figure 4. Fitting the EQE of the undoped cell in the GaAs wavelength region, we estimated a lower bound for the SRH lifetimes in the *p*-doped emitter and *n*-doped base of about 8 ns and 10 ns, respectively. For reference, the expected lifetimes, accounting for doping dependence, are about 20 ns and 300 ns, respectively [39]. Based on the model identified for the undoped cell, we have verified the impact of QD doping on J_{sc}. Since the actual distribution of dopant impurities is not known, we compare in Figure 4 different hypotheses of dopant distribution: dopant atoms at the QD site (direct doping), a thin layer of dopant atoms located in the middle of the interdot layer (mod. dop), and a uniform distribution across the whole QD stack. A detailed analysis of the impact of the different doping profiles on the energy band diagram and potential distribution may be found in [18]. Simulations in Figure 4 show that doping induces a clear penalty in the GaAs-range EQE, but such penalty is not sufficient to explain the reduced EQE of the direct doped samples with respect to the undoped ones. The EQE degradation is in fact reproduced by accounting for a reduction of minority carrier lifetime in the doped regions, with fitted SRH lifetimes of 500 ps in the emitter of the R5 sample and 50 ps (emitter)/200 ps (base) for the R4 sample.

Finally, the optical properties of the QD layer are estimated from the analysis of the subband gap EQE of the undoped cell reported in Figure 4(b). To this aim, the InAs/GaAs QD layer is described as a homogeneous equivalent medium with optical absorption $\alpha_{GaAs} + \Delta\alpha$ and real refractive index $n_{GaAs} + \Delta n$, where $\Delta\alpha$ and Δn are the absorption coefficient and refractive index of the QD material, weighted by the QD areal density. For the GS and ES states, a Gaussian distribution is used, with a peak absorption of 500 cm^{-1} and 1000 cm^{-1} and FWHM of 50 nm, respectively. The WL absorption profile is modeled by convolution of a Heaviside step function with a Lorentzian broadening function, with an absorption peak of about 2×10^4 cm^{-1} and FWHM of 40 nm. Representative examples of the spectral behavior of the extracted $\Delta\alpha$ and Δn can be found in [40]. The complex refractive index of bulk materials was taken from [41].

Figure 4(b) also highlights the suppression of QD photogeneration in the doped samples, with good agreement between measurements and simulations.

At open-circuit condition, based on the QD electronic model, we first analyze the predicted V_{oc} penalty of the QDSCs with respect to the bulk cell. To this aim, we take into account possible fluctuations of the QD confinement as seen from the PL spectra. Figure 6 reports the V_{oc} of the QD solar cell as a function of doping for different QD families with GS transition energy between 1.18 and 1.25 eV. SRH lifetimes in the doped regions are those extracted from the short-circuit analysis; in the undoped region, a SRH lifetime of 500 ns is assumed. For the sake of comparison, the V_{oc} (design value) of the REF cell is also reported. The analysis shows that the *inherent* (i.e., for negligible defectivity of the QD material) penalty due to the inclusion of the QDs is about 120 mV for the largest GS confinement, in agreement with previous theoretical works [20] and experimental data of QDSC with record V_{oc} [42]. Such penalty can be fully attributed

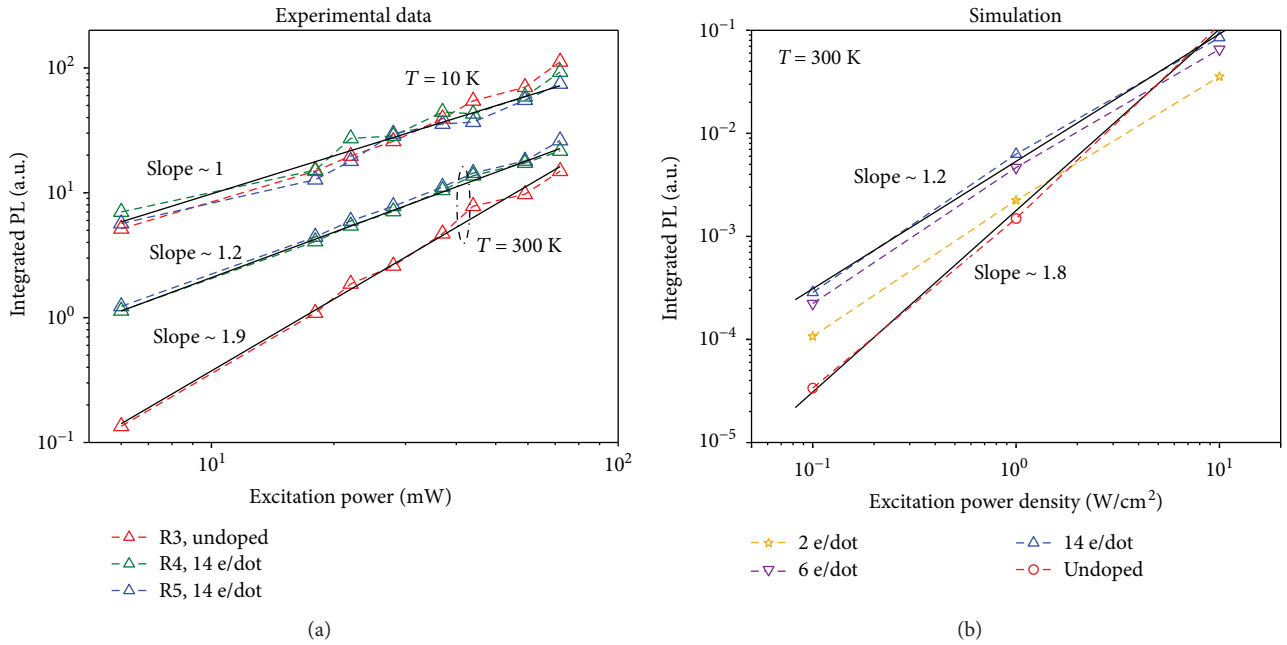

FIGURE 7: (a) Measured IPL intensity versus excitation power. (b) Simulated IPL intensity versus excitation power density. In the experiments, the equivalent excitation power density was about 1 W/cm^2 at power of 16 mW/cm^2.

to radiative recombination through the QD states [15, 18]. On the other hand, the comparison with the experimental data suggests that some other loss mechanism is in play in the devices under study, causing an added penalty of about 180 mV for the undoped case. Besides the measured data of the samples described in Section 3, we included also experimental data of very similar QDSCs, reported by the same research group in [43]. A very good agreement between simulated and measured data is obtained by assuming a significant defectivity of the interdot spacer layers, causing SRH lifetime (labeled as $\tau_{nr,QD}$ in Figure 6) on the order of fractions of ns, that is, lower than the QD radiative lifetime. The calculated trend of V_{oc} as a function of the doping density closely follows the measured one, suggesting that dopant atoms are well incorporated in the QDs and provide electrons per dot in line with the nominal doping value. Overall, the results highlight that doping is always beneficial in terms of V_{oc}, since it mitigates both QD radiative recombination and nonradiative recombination. QD radiative recombination is in fact suppressed by QD state filling; SRH recombination is suppressed because doping shifts the electron quasi-Fermi level far away from the intrinsic Fermi level reducing the capture/emission probability of electrons and holes by the midgap defect. Further analysis of doped-induced SRH suppression and examples of calculated SRH recombination rates in QDSCs may be found in [18, 44].

Finally, further supporting the interpretation that the QDSCs under study are limited by SRH recombination, Figure 7 compares the measured and simulated behavior of the integrated PL (IPL) versus the excitation power (P_{exc}): at $T = 10$ K, all the cells present a linear dependence of IPL with P_{exc} (slope ~ 1 in the log-log plot) regardless of doping, since they are dominated by the radiative recombination through the QDs. On the other hand, at $T = 300$ K, the undoped cell shows a superlinear dependence of IPL with P_{exc} (slope ~ 1.8 in the log-log plot), while the doped ones have again almost linear behavior. Our comprehension of the mechanism is that at $T = 300$ K nonradiative recombination through the barrier is an effective loss mechanism for photogenerated carriers that tends to be suppressed (or saturated) as the excitation power increases: thus, at low excitation power, IPL scales almost quadratically with P_{exc} [18, 45, 46]. The introduction of doping changes the electrostatic potential and electrical field profiles of the cell in such a way that SRH recombination results minimized. As a result, the doped QD cells have again a radiative limited behavior and their IPL scales linearly with P_{exc}.

5. Conclusion

We have applied physics-based numerical simulations to investigate the photovoltaic behavior of quantum dot solar cells which demonstrate a large increase of the open-circuit voltage with doping. The analysis of the experimental results points out that doping has profound effects on the cell behavior, which are difficult to disentangle without the support of device level simulations, since they involve the microscale, in terms of QD carrier dynamics, and the macroscale, since doping affects the electric field distribution across the photoactive region. The analysis allows also assessing the margin of improvement for the open-circuit voltage, taking into account that the cells under study operate under thermally limited regime; that is, two-step photon absorption is negligible. The presented device level simulations are developed within a multiscale modeling framework which combines in a self-consistent fashion transport equations in the bulk, rate equations for carrier dynamics in the QD states, and an accurate electromagnetic model of the optical field

across the cell. Further physical mechanisms relevant to QD-based solar cells, such as two-photon absorption, Auger processes, and hot carrier relaxation can be incorporated in this simulation framework allowing us to gain a deeper understanding of the physics of real devices and directions for their development.

Conflicts of Interest

The authors declare that they have no conflicts of interest.

Acknowledgments

This project has received funding from the European Union's Horizon 2020 Research and Innovation Programme under Grant Agreement no. 687253. F. Cappelluti acknowledges useful meetings and discussions supported by COST Action MP1406 "MultiscaleSolar".

References

[1] S. Hubbard and R. Raffaelle, "Boosting solar-cell efficiency with quantum-dot-based nanotechnology," *SPIE Newsroom*, 2010.

[2] A. Luque and A. Martí, "Increasing the efficiency of ideal solar cells by photon induced transitions at intermediate levels," *Physical Review Letters*, vol. 78, no. 26, pp. 5014–5017, 1997.

[3] S. Asahi, H. Teranishi, K. Kusaki, T. Kaizu, and T. Kita, "Two-step photon up-conversion solar cells," *Nature Communications*, vol. 8, p. 14962, 2017.

[4] D. M. Tex, I. Kamiya, and Y. Kanemitsu, "Control of hot-carrier relaxation for realizing ideal quantum-dot intermediate-band solar cells," *Scientific Reports*, vol. 4, p. 4125, 2014.

[5] U. Aeberhard, "Simulation of nanostructure-based high-efficiency solar cells: challenges, existing approaches, and future directions," *IEEE Journal of Selected Topics in Quantum Electronics*, vol. 19, no. 5, pp. 1–11, 2013.

[6] M. Y. Levy and C. Honsberg, "Solar cell with an intermediate band of finite width," *Physical Review B*, vol. 78, no. 16, article 165122, 2008.

[7] L. Cuadra, A. Marti, and A. Luque, "Influence of the overlap between the absorption coefficients on the efficiency of the intermediate band solar cell," *IEEE Transactions on Electron Devices*, vol. 51, no. 6, pp. 1002–1007, 2004.

[8] R. Strandberg and T. Reenaas, "Optimal filling of the intermediate band in idealized intermediate-band solar cells," *IEEE Transactions on Electron Devices*, vol. 58, no. 8, pp. 2559–2565, 2011.

[9] V. Aroutiounian, S. Petrosyan, A. Khachatryan, and K. Touryan, "Quantum dot solar cells," *Journal of Applied Physics*, vol. 89, no. 4, pp. 2268–2271, 2001.

[10] A. S. Lin and J. D. Phillips, "Drift-diffusion modeling for impurity photovoltaic devices," *IEEE Transactions on Electron Devices*, vol. 56, no. 12, pp. 3168–3174, 2009.

[11] K. Yoshida, Y. Okada, and N. Sano, "Self-consistent simulation of intermediate band solar cells: effect of occupation rates on device characteristics," *Applied Physics Letters*, vol. 97, no. 13, p. 133503, 2010.

[12] I. Tobías, A. Luque, and A. Martí, "Numerical modeling of intermediate band solar cells," *Semiconductor Science and Technology*, vol. 26, no. 1, article 014031, 2011.

[13] R. Strandberg and T. Reenaas, "Drift-diffusion model for intermediate band solar cells including photofilling effects," *Progress in Photovoltaics*, vol. 19, no. 1, pp. 21–32, 2012.

[14] V. Aroutiounian, S. Petrosyan, and A. Khachatryan, "Studies of the photocurrent in quantum dot solar cells by the application of a new theoretical model," *Solar Energy Materials and Solar Cells*, vol. 89, no. 2, pp. 165–173, 2005.

[15] M. Gioannini, A. P. Cedola, N. Di Santo, F. Bertazzi, and F. Cappelluti, "Simulation of quantum dot solar cells including carrier intersubband dynamics and transport," *IEEE Journal of Photovoltaics*, vol. 3, no. 4, pp. 1271–1278, 2013.

[16] M. Gioannini, A. P. Cedola, and F. Cappelluti, "Impact of carrier dynamics on the photovoltaic performance of quantum dot solar cells," *IET Optoelectronics*, vol. 9, no. 2, pp. 69–74, 2015.

[17] T. Sogabe, Q. Shen, and K. Yamaguchi, "Recent progress on quantum dot solar cells: a review," *Journal of Photonics for Energy*, vol. 6, no. 4, article 040901, 2016.

[18] F. Cappelluti, M. Gioannini, and A. Khalili, "Impact of doping on InAs/GaAs quantum-dot solar cells: a numerical study on photovoltaic and photoluminescence behavior," *Solar Energy Materials and Solar Cells*, vol. 157, pp. 209–220, 2016.

[19] D. Bimberg, M. Grundmann, and N. N. Ledentsov, *Quantum Dot Heterostructures*, John Wiley & Sons, 1999.

[20] G. Jolley, L. Fu, H. F. Lu, H. H. Tan, and C. Jagadish, "The role of intersubband optical transitions on the electrical properties of InGaAs/GaAs quantum dot solar cells," *Progress in Photovoltaics*, 2012.

[21] G. A. Kosinovsky, "Threshold current and modulation response of semiconductor lasers," PhD Thesis, 1995.

[22] T. R. Nielsen, P. Gartner, and F. Jahnke, "Many-body theory of carrier capture and relaxation in semiconductor quantum-dot lasers," *Physical Review B*, vol. 69, no. 23, article 235314, 2004.

[23] G. A. Narvaez, G. Bester, and A. Zunger, "Carrier relaxation mechanisms in self-assembled (In, Ga) As/Ga As quantum dots: efficient $P \rightarrow S$ Auger relaxation of electrons," *Physical Review B*, vol. 74, no. 7, article 075403, 2006.

[24] K. Schuh, P. Gartner, and F. Jahnke, "Combined influence of carrier-phonon and coulomb scattering on the quantum-dot population dynamics," *Physical Review B*, vol. 87, no. 3, article 035301, 2013.

[25] S. Tomić, "Intermediate-band solar cells: influence of band formation on dynamical processes in InAs/GaAs quantum dot arrays," *Physical Review B*, vol. 82, no. 19, article 195321, 2010.

[26] J. Siegert, S. Marcinkevičius, and Q. X. Zhao, "Carrier dynamics in modulation-doped InAs/GaAs quantum dots," *Physical Review B*, vol. 72, no. 8, 2005.

[27] F. Cappelluti, A. Khalili, and M. Gioannini, "Open circuit voltage recovery in quantum dot solar cells: a numerical study on the impact of wetting layer and doping," *IET Optoelectronics*, vol. 11, no. 2, pp. 44–48, 2017.

[28] P. W. Fry, J. J. Finley, L. R. Wilson et al., "Electric-field-dependent carrier capture and escape in self-assembled InAs/GaAs quantum dots," *Applied Physics Letters*, vol. 77, no. 26, pp. 4344–4346, 2000.

[29] T. Müller, F. Schrey, G. Strasser, and K. Unterrainer, "Ultrafast intraband spectroscopy of electron capture and relaxation in InAs/GaAs quantum dots," *Applied Physics Letters*, vol. 18, no. 17, pp. 3572–3574, 2003.

[30] L. A. Pettersson, L. S. Roman, and O. Inganäs, "Modeling photocurrent action spectra of photovoltaic devices based on organic thin films," *Journal of Applied Physics*, vol. 86, no. 1, pp. 487–496, 1999.

[31] F. Bertazzi, F. Cappelluti, S. D. Guerrieri, F. Bonani, and G. Ghione, "Self-consistent coupled carrier transport full-wave EM analysis of semiconductor traveling-wave devices," *IEEE Transactions on Microwave Theory and Techniques*, vol. 54, no. 4, pp. 1611–1618, 2006.

[32] D. Kim, M. Tang, J. Wu et al., "Si-doped InAs/GaAs quantum-dot solar cell with AlAs cap layers," *IEEE Journal of Photovoltaics*, vol. 6, no. 4, pp. 906–911, 2016.

[33] H. Y. Liu, I. R. Sellers, T. J. Badcock et al., "Improved performance of 1.3μm multilayer InAs quantum-dot lasers using a high-growth-temperature GaAs spacer layer," *Applied Physics Letters*, vol. 85, no. 5, pp. 704–706, 2004.

[34] H. Y. Liu, S. L. Liew, T. Badcock et al., "p-doped 1.3μm InAs/GaAs quantum-dot laser with a low threshold current density and high differential efficiency," *Applied Physics Letters*, vol. 89, no. 7, article 073113, 2006.

[35] F. K. Tutu, I. R. Sellers, M. G. Peinado et al., "Improved performance of multilayer InAs/GaAs quantum-dot solar cells using a high-growth-temperature GaAs spacer layer," *Journal of Applied Physics*, vol. 111, no. 4, article 046101, 2012.

[36] M. Wolf and H. Rauschenbach, "Series resistance effects on solar cell measurements," *Advanced Energy Conversion*, vol. 3, no. 2, pp. 455–479, 1963.

[37] H. L. Wang, F. H. Yang, and S. L. Feng, "Photoluminescence in Si and Be directly doped self-organized InAs/GaAs quantum dots," *Journal of Crystal Growth*, vol. 212, no. 1-2, pp. 35–38, 2000.

[38] A. Markus, M. Rossetti, V. Calligari, J. Chen, and A. Fiore, "Role of thermal hopping and homogeneous broadening on the spectral characteristics of quantum dot lasers," *Journal of Applied Physics*, vol. 98, no. 10, article 104506, 2005.

[39] M. P. Lumb, M. A. Steiner, J. F. Geisz, and R. J. Walters, "Incorporating photon recycling into the analytical drift-diffusion model of high efficiency solar cells," *Journal of Applied Physics*, vol. 116, no. 19, article 194504, 2014.

[40] A. Musu, F. Cappelluti, T. Aho, V. Polojärvi, T. K. Niemi, and M. Guina, "Nanostructures for light management in thin-film GaAs quantum dot solar cells," in *Solid-State Lighting*, no. article JW4A.45, 2016Optical Society of America, 2016.

[41] Sopra database. 1995-2016 Software Spectra, Inc.http://sspectra.com/sopra.html.

[42] C. G. Bailey, D. V. Forbes, R. P. Raffaelle, and S. M. Hubbard, "Near 1 V open circuit voltage InAs/GaAs quantum dot solar cells," *Applied Physics Letters*, vol. 98, no. 16, article 163105, 2011.

[43] P. Lam, S. Hatch, J. Wu et al., "Voltage recovery in charged InAs/GaAs quantum dot solar cells," *Nano Energy*, vol. 6, pp. 159–166, 2014.

[44] S. J. Polly, D. V. Forbes, K. Driscoll, S. Hellstrom, and S. M. Hubbard, "Delta-doping effects on quantum-dot solar cells," *IEEE Journal of Photovoltaics*, vol. 4, no. 4, pp. 1079–1085, 2014.

[45] S. Sanguinetti, D. Colombo, M. Guzzi et al., "Carrier thermodynamics in InAs/$In_xGa_{1-x}As$ quantum dots," *Physical Review B*, vol. 74, no. 20, article 205302, 2006.

[46] T. Kita, R. Hasagawa, and T. Inoue, "Suppression of nonradiative recombination process in directly Si-doped InAs/GaAs quantum dots," *Journal of Applied Physics*, vol. 110, no. 10, article 103511, 2011.